

Lattice stabilization and strain homogenization in Sn-Pb bottom subcells enable stable all-perovskite tandems solar cells

Received: 29 May 2025

Accepted: 28 July 2025

Published online: 09 August 2025



Yang Bai^{1,2,4,5}, Yuanyuan Meng^{1,4,5}, Ming Yang^{1,4,5}, Ruijia Tian¹, Jingnan Wang¹, Boxin Jiao³, Haibin Pan¹, Jiangwei Gao¹, Yaohua Wang¹, Kexuan Sun¹, Shujing Zhou¹, Xiaoyi Lu¹, Zhenhua Song¹, Chang Liu^{1,2,5} ✉ & Ziyi Ge^{1,2,5} ✉

All-perovskite tandem solar cells (PTSCs) offer a promising approach to surpass the Shockley-Queisser (SQ) limit, driven by efficiently reducing thermalization and transmission losses. However, the efficiency and stability of the narrow-bandgap (NBG) subcells, which are essential for PTSC performance, remain severely constrained by challenges such as lattice instability, strain accumulation and halide migration under illumination. This study introduces a rigid sulfonate-based molecule, sodium naphthalene-1,3,6-trisulfonate (NTS), into tin-lead (Sn-Pb) perovskites, where it strengthens the Sn-I bond through Sn-trisulfonate coordination and reduces light-induced dynamic lattice distortions via the rigid NTS backbone. These molecular interactions alleviate strain heterogeneity within the lattice and homogenize the Sn-Pb compositional gradient, thereby enhancing the structural integrity and long-term stability of Sn-Pb perovskites under operational conditions. As a result, Sn-Pb single-junction perovskite solar cells (PSCs) achieve a power conversion efficiency (PCE) of 23.2%. When integrated into a tandem configuration, the device attains an impressive PCE of 29.6% (certified PCE of 29.2%, one of the highest certified efficiencies to date), with 93.1% of the initial efficiency retained after 700 h of continuous operation. By stabilizing the lattice structure, this work lays a solid foundation for achieving both high efficiency and long-term durability in next-generation perovskite photovoltaics.

Organic-inorganic hybrid perovskite solar cells (PSCs) have revolutionized the field of photovoltaics, achieving up to 26.7% power conversion efficiency (PCE) in single-junction devices^{1–4}. All-perovskite tandem solar cells (PTSCs) further hold the potential

to exceed the Shockley-Queisser (SQ) limit by reducing both thermalization and transmission losses^{5–9}. However, the efficiency and stability of narrow-bandgap (NBG) subcells, crucial for PTSCs, remain constrained by issues like defect

¹Zhejiang Provincial Engineering Research Center of Energy Optoelectronic Materials and Devices, Ningbo Institute of Materials Technology & Engineering, Chinese Academy of Sciences, Ningbo, China. ²Center of Materials Science and Optoelectronics Engineering, University of Chinese Academy of Sciences, Beijing, China. ³State Key Laboratory of Power System, Department of Electrical Engineering, Tsinghua University, Beijing, China. ⁴These authors contributed equally: Yang Bai, Yuanyuan Meng, Ming Yang. ⁵These authors jointly supervised this work: Chang Liu, Ziyi Ge. ✉e-mail: liuchang1@nimte.ac.cn; geziyi@nimte.ac.cn

formation, halide migration, and lattice instability during operation^{10–19}.

An in-depth understanding of light-induced lattice oscillations is essential to address these challenges and ensure the long-term stability and performance of NBG PSCs. In pure tin (Sn)-based perovskite system, light-induced lattice expansion arises primarily from dynamic perturbations triggered by strong electron-phonon coupling involving Sn^{2+} cations and photothermal effects^{20–22}. Illumination enhances anharmonic thermal vibrations²³, destabilizing the Sn-I bond, which undergoes periodic oscillations and, under high excitation, potential cleavage. This localized lattice expansion facilitates ion migration and rapid formation of iodide vacancies (V_I). High photogenerated carrier concentrations further intensify the oxidative instability of Sn^{2+} , amplifying lattice distortion and accelerating structural degradation. This arises from carrier-assisted iodide migration and redox reactions, as well as strong coupling between photocarriers and lattice vibrations that promote strain buildup and bond weakening^{24–27}. In contrast, lead (Pb)-based perovskites exhibit lattice expansion predominantly governed by photothermal effects²⁸. The inert pair effect and low oxidation sensitivity of Pb^{2+} confer structural stability under illumination, with Pb-I bonds demonstrating minimal length changes due to their high dissociation energy and low vibrational amplitude. This stability ensures the long-term structural and optoelectronic reliability of Pb-based perovskites²¹.

Sn-Pb perovskites present unique opportunities and challenges due to the interplay of Pb and Sn. While Pb enhances the oxidative stability of Sn^{2+} and mitigates I^- migration, the lattice dynamics exhibit complex many-body effects^{29–31}. Variations in electron-phonon coupling (EPC) strength between Pb^{2+} and Sn^{2+} cations can lead to spatial differences in carrier-lattice interactions, which in turn contribute to lattice heterogeneity and localized stress concentrations exceeding those in pure Sn-based systems^{32,33}. These stress points reflect the structural heterogeneity of the material, with Sn-I bonds remaining vulnerable to rupture under illumination. This exacerbates interfacial stress heterogeneity, leading to permanent lattice distortions over time and impairing device performance and longevity. Though various attempts have been made to tackle the instability challenges of Sn-Pb perovskites through additive molecular engineering, optimization of precursor chemistry, introduction of multifunctional interfacial modifiers, advanced additive strategies, etc., the susceptibility of Sn-I bonds to dynamic strain and ion migration necessitates more targeted approaches to further enhance lattice stability^{27,34–38}.

Recent progress in Sn-Pb perovskites has revealed a complex degradation landscape governed by Sn^{2+} oxidation, asynchronous Sn/Pb crystallization, and light- or thermally induced lattice destabilization^{8,14,34,36,39–44}. To mitigate these instabilities, diverse strategies have been developed, including reductive additives, interfacial passivation, solvent coordination tuning, and phase-selective crystallization control. While these approaches have improved performance to some extent, they often target isolated degradation pathways and fail to address the root cause, which is light-induced dynamic strain and bond weakening in the Sn-I framework. This study aims to address these issues by exploring targeted molecular interactions to improve lattice stability in Sn-Pb perovskites. Sulfonate-containing ions were chosen for their strong coordination with Sn^{2+} cation to reinforce the Sn-I bond. Sulfonate-containing compounds with different structural rigidity, including alkyl-chain based sodium dodecyl sulfate (SDS), phenyl-based sodium benzenesulfonate (SBS), naphthyl based 1-sulfonate (NSA), sodium naphthalene-2,6-disulfonate (NDS), and sodium naphthalene-1,3,6-trisulfonate (NTS) (molecular structures are illustrated in Supplementary Fig. 1 and Fig. 1a) were systematically evaluated for their impact on Sn-I bond stabilization, lattice vibrations and electron-phonon coupling dynamics. From combined results of *ab initio* molecular dynamics (AIMD) simulations and Raman spectroscopy, it is found that highly rigid naphthyl derivative with multiple

sulfonate anchors shows the strongest cohesion to perovskite lattices, which minimizes dynamic distortions and prevents bond elongation under illumination. This helps maintaining lattice symmetry and alleviates the strain heterogeneity, leading to less tendency of Sn-I bond rupture and prevents the subsequent formation of I-vacancies. The target Sn-Pb NBG film thus shows superior thermal and light resilience. As a result, the NTS treated NBG subcell achieves significantly improved PCE from 21.3% (control) to 23.2%, with 94.1% of the initial PCE retained after 750 h maximum power point (MPP) tracking. Integrated with a wide-bandgap (WBG) perovskite, the 2-terminal (2T) PTSCs demonstrate an impressive PCE of 29.6% (certified PCE of 29.2%, one of the highest certified values), retaining 93.1% of the initial PCE after 700 h of MPP tracking.

Results

Controlling lattice expansion via Sn-I bond strengthening

Raman spectroscopy was used to systematically study the effect of sulfonate groups on the stability of lattice framework in different systems. By monitoring wavenumber shifts in Sn-I and Pb-I bonds under various illumination conditions, the analysis reveals how bond strength evolves, providing insights into the stability of Sn-I and Pb-I bonds under light exposure^{23,45}. Raman spectroscopy (Supplementary Fig. 2 and Fig. 1b–d) of Sn-Pb perovskite films under varying light exposure durations (0, 5, 10, and 15 h) elucidates the structural dynamics of control film and films treated with five different additives. Vibrational peaks at 76–81 cm^{-1} and 115–125 cm^{-1} are assigned to Pb-I and Sn-I bonding modes, respectively. These peaks serve as indicators of the local bonding environment, as shifts in vibrational frequency are directly correlated with changes in bond strength and electron cloud distribution. In the control film, the Pb-I and Sn-I vibrational peaks are initially located at 80.0 cm^{-1} and 118.2 cm^{-1} , respectively. Upon incorporating SDS, SBS, NSA, and NDS, these peaks shift to higher wavenumbers of 80.1, 80.3, 80.6, 80.9, and 80.9 cm^{-1} for Pb-I; and 120.2, 120.2, 120.7, 120.8, and 120.9 cm^{-1} for Sn-I. These results indicate that sulfonate groups coordinate with Sn^{2+} and Pb^{2+} via electron donation, thereby modulating the local electronic environment and enhancing the covalent character of the Sn-I and Pb-I bonds. This interaction redistributes electron density around the metal centers and stabilizes bonding orbitals, resulting in stronger bonding interactions. These strengthened bonds are spectroscopically manifested as blue-shifts in the characteristic Sn-I and Pb-I vibrational modes. After 5 and 10 h of illumination in the control film, the Sn-I peak shifts to lower wavenumbers by 0.9 cm^{-1} and 2.1 cm^{-1} , respectively, while the Pb-I peak shifts to lower wavenumbers by 0.2 cm^{-1} and 1.7 cm^{-1} , respectively. These changes could be attributed to the bond elongation and thermal expansion caused by photon energy, reducing bond stability. Notably, a split of Sn-I peak, suggestive of a partial bond rupture, is observed upon 20 h illumination, which likely introduces structural defects and disrupts the electronic symmetry of the perovskite lattice. In contrast, the Pb-I peak remains intact, confirming the greater robustness of Pb-I bonds in Sn-Pb perovskites. Among the five additives, NTS incorporation shows the least displacements in Sn-I and Pb-I peaks, with downward shifts of only 0.1 cm^{-1} and 0.4 cm^{-1} , respectively, after 20 h illumination. These results indicate that NTS, with multiple sulfonate anchors, effectively reinforces the Sn-I bond. Additionally, the highly rigid naphthalene minimizes light-induced bond length fluctuations and mitigates strain heterogeneity within lattice, demonstrating its ability to withstand thermal stress and resist structural perturbations induced by photon energy. Comparatively, the more flexible alkyl chain of SDS shows higher tendency of bond deformation. This stabilization preserves lattice symmetry and reduces the probability of defect formation. Furthermore, it prevents fragmentation of the Sn-I network and suppresses ion migration, both of which are critical factors in the degradation of optoelectronic properties in long-term state.

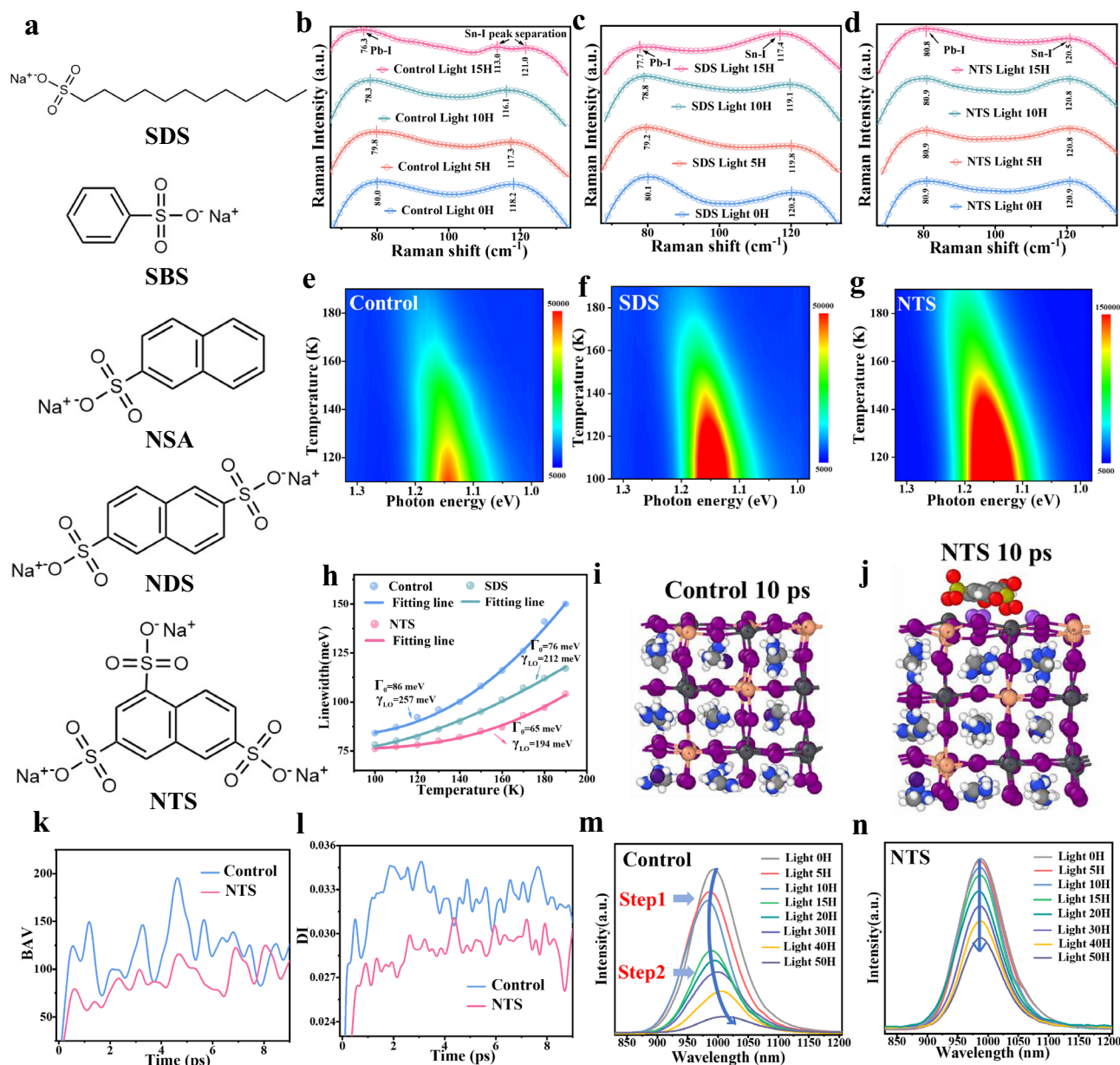


Fig. 1 | Controlling lattice expansion via Sn-I bond strengthening. **a** Chemical structures of SDS, SBS, NSA, NDS and NTS. **b–d** Raman spectra of the control, SDS and NTS modified films. **e–g** Pseudo-color maps of temperature-dependent photoluminescence (TD-PL) spectra for the control, with SDS, and with NTS films across a temperature range of 100–190 K. **h** Temperature dependence of the full width at half maximum (FWHM) of PL peaks for the respective films. **i, j** Schematic

representations of lattice distortions under AIMD simulations at 10 ps for the control and films incorporating NTS. **k, l** Computational results for bond angle variance (BAV) and distortion index (DI) to quantify lattice distortions. **m, n** Photoluminescence (PL) spectra of the control and films modified with NTS under different aging conditions (0–50 h of continuous light exposure).

To further validate the cooperative coordination behavior of sulfonate groups, we conducted concentration-dependent Raman measurements using mono-, di-, and tri-sulfonate molecules (NSA, NDS, and NTS, respectively; Supplementary Fig. 3). At equivalent concentrations, the Sn-I vibrational blue-shift scales with the number of sulfonate anchors, reaching up to 119.5 cm^{-1} in NTS-treated films. Moreover, NTS exhibits saturation of the blue-shift at 0.6 mg mL^{-1} , while NSA and NDS continue to shift at higher concentrations. These trends confirm that NTS engages in efficient tridentate coordination with Sn^{2+} centers, saturating available binding sites and providing superior lattice stiffening.

In addition to vibrational analysis, spectroscopic evidence confirms the formation of Sn-O coordination bonds upon sulfonate incorporation. A distinct vibrational mode near 500 cm^{-1} appears

exclusively in NDS- and NTS-treated films (Supplementary Fig. 4), which is absent in the control. This feature is attributed to the stretching vibration of Sn–O bonds, indicating that sulfonate oxygen atoms coordinate directly with Sn^{2+} sites. These interactions involve electron donation from the sulfonate groups to the Sn 5s/5p orbitals, stabilizing the electronic structure of Sn^{2+} and reducing the stereochemical activity of its lone pair. As a result, the local bonding environment is reinforced, contributing to the structural robustness of the perovskite lattice.

To further quantify the influence of sulfonate coordination on Sn-I bonding, we performed crystal orbital Hamilton population (COHP) analysis to probe the electronic structure at the bond level. The integrated -COHP (-ICOHP) values for Sn-I bonds increase from 2.35 eV in the control film to 2.45 eV with SDS and 2.74 eV with NTS treatment

(Supplementary Fig. 5), reflecting a progressive enhancement in bond strength. This strengthening arises from the electronic effects of sulfonate coordination, which lower the population of antibonding Sn-I states near the Fermi level and enhance orbital overlap within the bonding states. The resulting increase in covalent character is consistent with the observed Raman blue-shifts and reduced vibrational disorder under illumination. Taken together, these results demonstrate that sulfonate additives, especially rigid multidentate molecules such as NTS, enhance Sn-I bond stability through direct electronic stabilization and coordination-driven modulation of the local bonding environment.

To further dig into the structural rigidity of sulfonate-contained additives on affecting the lattice vibrations in Sn-Pb perovskites, phonon couplings in the NBG films were investigated by temperature-dependent photoluminescence (TD-PL) measurements on pristine, SDS-treated, and NTS-treated films. In organometallic halide perovskites, electron-phonon coupling is predominantly governed by Fröhlich interactions between longitudinal optical (LO) phonons and electrons. According to the Bose-Einstein thermal distribution, $\Gamma(T) = \Gamma_0 + \Gamma_{LO}(T) = \Gamma_0 + \frac{\gamma_{LO}}{e^{\gamma_{LO}/kT} - 1}$ where Γ_0 represents inhomogeneous broadening unrelated to temperature and Γ_{LO} corresponds to temperature-dependent homogeneous broadening, the broadening of PL spectra is attributed to the interactions between LO phonons and electrons^{46–48}. By analyzing the full-width at half-maximum (FWHM) of PL spectra across temperatures (Fig. 1e–g), the coupling strength γ_{LO} was extracted. The extracted γ_{LO} values decrease from 257 meV in the pristine film to 212 meV with SDS and 194 meV with NTS treatment (Fig. 1h), indicating a progressive suppression of exciton–phonon interactions. This trend reflects increased lattice rigidity rather than weakened chemical bonding, limiting vibrational coupling. In metal halide perovskites, γ_{LO} serves as an indicator for lattice softness: more deformable, dynamically disordered lattices exhibit stronger phonon scattering, while rigid lattices suppress low-frequency fluctuations and polar lattice responses^{49–51}.

To directly correlate these spectroscopic trends with local mechanical properties, we performed PeakForce Quantitative Nano-mechanical Mapping (PF-QNM) on films incorporating different sulfonate additives (Supplementary Fig. 6). The control film displays low and spatially heterogeneous modulus values, consistent with a mechanically soft and disordered structure. SDS-treated films exhibit a modest modulus increase, while NDS and NTS yield significantly stiffer domains, with elastic moduli exceeding 10 GPa in the latter. This monotonic increase in mechanical stiffness across the additive series mirrors the observed decrease in γ_{LO} , establishing a direct structure–property relationship.

Together, the TD-PL and QNM results demonstrate that sulfonate-induced lattice stiffening, particularly from rigid, multidentate molecules such as NTS, effectively suppresses phonon-mediated exciton scattering. This reduced exciton–phonon interaction contributes to enhanced optoelectronic stability by minimizing dynamic lattice disorder, and further reinforces the role of additive-enabled lattice rigidity as a central mechanism for light-induced degradation resistance in Sn-Pb perovskites.

AIMD simulations were conducted to evaluate the structural evolution of the perovskite lattice under thermal stress at specific time intervals (0 ps, 2.5 ps, 5.0 ps, 7.5 ps, and 10.0 ps), the results are shown in Supplementary Fig. 7 and Fig. 1i–g. In the control system, significant lattice distortions are observed as early as 2.5 ps, characterized by pronounced elongation and angular deviations in the octahedral framework of Pb-I and Sn-I bonds. These distortions progressively worsened at 5.0 ps and 7.5 ps, ultimately resulting in extensive structural irregularities, broken bonds, and considerable ionic movements at 10.0 ps. Conversely, the NTS-treated system demonstrates remarkable lattice stability, with the octahedral geometry remaining intact even after 10.0 ps. Building on these findings, root mean square deviation

(RMSD) calculations were performed for the 0–9 ps time range using the relaxed 1 ps structure as the reference frame. In the NTS-treated system, I-RMSD values are significantly lower than those of the control system, indicating that NTS effectively suppresses iodide ion migration and mitigates lattice distortions. Meanwhile, the RMSD values for Sn and Pb exhibit only marginal decreases in the NTS-treated system relative to the control one. This behavior can be attributed to the inherently lower mobility of the larger Sn and Pb cations within the lattice, while the slight reduction suggests that the cation sublattice still benefits from the stabilizing influence of the NTS additive (Supplementary Fig. 8).

To further assess lattice distortion, distortion index (DI) and bond angle variance (BAV) analyses were conducted over the same 0–9 ps time range (Fig. 1k, l). DI quantifies variations in Pb-I and Sn-I bond lengths, with higher values indicating greater lattice irregularities⁵². BAV measures deviations of the Pb-I and Sn-I octahedra from ideal lattice geometry, with larger values reflecting greater structural distortions⁵². The simulation results demonstrate that the DI and BAV values in the NTS-treated system are significantly lower than those in the control system, underscoring the role of NTS in minimizing Pb-I and Sn-I bond fluctuations and preserving the octahedral geometry. This enhanced lattice stability highlights the effectiveness of NTS in mitigating structural distortions and ensuring a robust perovskite framework under operational conditions.

Photoluminescence (PL) spectra of the control film (Fig. 1m) reveal that under long-term illumination, bandgap of Sn-Pb perovskites undergoes a two-phase evolution, with the PL peak initially blue-shifting (Step 1: 0–15 h) and subsequently red-shifting (Step 2: after 15 h). During Step 1, the increment in bandgap could be attributed to enhanced vibrational energy within the Sn-I and Pb-I bonds caused by thermal excitation, which intensifies local atomic oscillations. This would also introduce slight lattice mismatches due to different thermal responsivity of Sn-I and Pb-I bonds, leading to temporal lattice distortions that widen the bandgap^{53,54}.

As illumination progresses into Step 2, cumulative photon-induced lattice stress and thermal expansion destabilize the structural framework of the perovskite. The accumulation of strain alters lattice constants, promotes defect formation, and weakens local bonding. During this stage, the PL peak undergoes a red-shift, which may arise from a combination of two mechanisms: (1) progressive narrowing of the intrinsic bandgap due to irreversible lattice distortion and Sn-I bond weakening, and (2) the formation of shallow non-radiative trap states is likely associated with halide vacancies, Sn^{2+} oxidation, and local disorder at grain boundaries, all of which become more pronounced under prolonged illumination. Raman analysis reveals that Sn-I bond rupture coincides with this phase, facilitating the emergence of iodide vacancies and Sn^{4+} centers that further exacerbate structural instability and deepen trap state distributions. As defect accumulation intensifies, the crystal lattice experiences microscopic collapse, resulting in further bandgap reduction and increased non-radiative recombination^{55,56}. In comparison, SDS-treated films (Supplementary Fig. 9) exhibit a similar two-phase PL evolution but with attenuated shifts in both directions, indicating partial suppression of photon-induced stress and defect formation. In contrast, NTS-treated films (Fig. 1n) demonstrate exceptional photostability, with negligible PL peak shift throughout prolonged illumination. This behavior suggests that NTS coordination effectively mitigates both lattice deformation and the formation of defect states, thereby stabilizing the optoelectronic structure of the perovskite under operational conditions.

X-ray diffraction (XRD) analysis further elucidates the structural evolution underlying the two-phase bandgap dynamics observed in PL measurements. In the control film (Supplementary Fig. 10a), the (100) diffraction peak gradually shifts toward lower angles during the initial 15 h of illumination, consistent with lattice

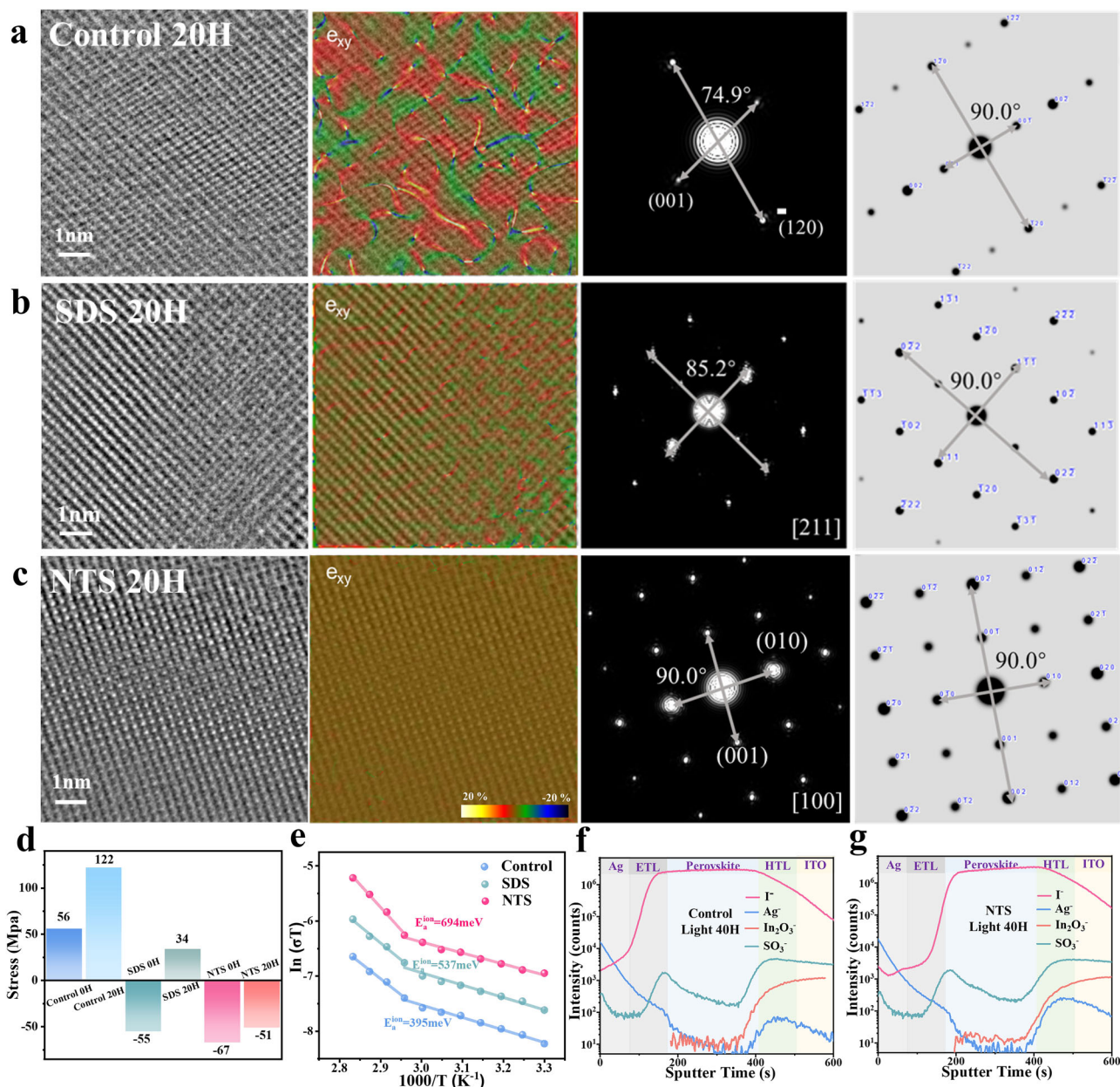


Fig. 2 | Regulating lattice strain to suppress ion migration. Integrated differential phase contrast (IDPC) images, geometric phase analysis (GPA) strain maps (e_{xy}), and fast Fourier transform (FFT) patterns of the perovskite lattice for **a** control, **b** SDS modified, and **c** NTS modified films after 20 h of light exposure. **d** Stress statistics of control, SDS modified, and NTS modified perovskite films

before and after 20 h of illumination, derived from Grazing incidence X-ray diffraction (GIXRD) analysis. **e** Arrhenius plots of conductivity for control, SDS modified, and NTS modified perovskite films. Time-of-flight secondary ion mass spectrometry (TOF-SIMS) depth profiles of halide migration under light 40 h for **f** pristine perovskite film and **g** perovskite film with NTS.

expansion driven by photon-induced thermal and structural perturbations. This behavior aligns with the initial PL blueshift, reflecting localized lattice mismatch and transient distortion. However, after 20 h of illumination, the diffraction peak shifts sharply to approximately 13.4° , indicating the collapse of the lattice structure and the formation of a degraded phase⁵⁷. This phase transition is driven by irreversible lattice contraction and severe structural distortion, primarily caused by cumulative Sn-I bond breakage and localized stress exceeding the lattice's elastic limit²³. In contrast, the NTS-treated films demonstrate exceptional lattice stability, with negligible shift of (100) plane even after prolonged illumination (Supplementary Fig. 10c). It suggests the ability of NTS to effectively suppress the collapse of Sn-Pb perovskite phase by reinforcing Sn-I bonds and mitigating photon-induced strain.

Meanwhile, the SDS-treated films exhibit moderate stability, characterized by small displacements of the (100) diffraction peak, indicating that the flexible alkyl structures provide limited protection against lattice distortions under prolonged illumination.

Regulating lattice strain to suppress ion migration

To investigate the structural evolution and strain accumulation in Sn-Pb perovskites during prolonged illumination, transmission electron microscopy (TEM) analysis was performed using the ultra-low dose rate Integrated Differential Phase Contrast (IDPC) mode to avoid electron beam damage, enabling high-resolution imaging of the lattice structure and direct visualization of structural degradation at the atomic scale^{58–60}. The TEM results reveal substantial differences in lattice stability among the control, SDS-treated, and NTS-treated films,

as shown in and Fig. 2a–c. IDPC images of the control film after 20 h of illumination demonstrate severe lattice distortion relative to the fresh film (Supplementary Fig. 11), providing clear evidence of lattice collapse⁶⁰. The geometric phase analysis (GPA) strain maps of the control, SDS-modified, and NTS-modified perovskite films illustrate the strain components, as presented in Supplementary Fig. 12 and Fig. 2a–c. The shear strain maps reveal significant strain concentrations in the control film, with red-dominated regions indicating localized strain accumulation, which ultimately drives structural collapse. In the SDS modified film, moderate lattice stability is observed. IDPC images in Fig. 2b reveal a notably relieved lattice degradation, though residual strain heterogeneity persists. In contrast, the NTS modified film exhibits exceptional lattice stability and structural integrity. IDPC images show highly ordered lattice arrangements, and strain mapping reveals uniform strain distribution with minimal areas of high-strain concentration. Fast Fourier Transform (FFT) patterns further corroborate these findings⁶¹. In the control film, the FFT patterns exhibit fuzzy and asymmetric diffraction spots, indicating reduced crystallinity and the formation of a disordered phase after prolonged illumination. A comparison with indexed standard FFT patterns confirms significant deviations in the diffraction angle, particularly in the control film, where the angles deviate substantially from the ideal 90°, reflecting a loss of lattice symmetry and severe structural distortion. The SDS-treated film shows diffraction angle approaching 90°, although slight angular deviations remain, suggesting that the flexible alkyl chains of SDS offer limited protection against photon-induced lattice distortions. In stark contrast, the FFT pattern of the NTS-treated film displays sharp, symmetrical diffraction spots with diffraction angles precisely at 90°, confirming the complete preservation of crystallinity and lattice symmetry even under long-term illumination. These results underscore the efficacy of NTS in suppressing strain propagation and lattice destabilization through its rigid molecular framework, effectively maintaining the structural and optoelectronic stability of Sn-Pb perovskites.

How the above observed local strain concentrations affect the overall stress distribution requires further study^{21,62,63}. Grazing incidence X-ray diffraction (GIXRD) was adopted to quantify the stress distribution in the film. In the control film, the stress state remains tensile both before and after illumination, with a significant increment over time (Supplementary Figs. 13, 14 and Fig. 2d). Initially, the film exhibits tensile stress of +56 MPa, likely caused by residual stresses from the film deposition process, such as incomplete thermal relaxation or lattice mismatch between the perovskite layer and the substrate. After 20 h illumination, the tensile stress escalates dramatically to +122 MPa, driven by photon-induced expansion. The pronounced increment is closely associated with the structural collapse revealed by TEM, highlighting the effects of stress accumulation on destabilizing the lattice framework.

By contrast, the SDS- and NTS-treated films exhibit compressive stress in the absence of illumination, measured at –55 MPa and –67 MPa, respectively. Compressive stress plays a pivotal role in stabilizing the perovskite lattice, as it suppresses lattice vibrations and inhibits defect migration, thereby reducing dynamic structural fluctuations and enhancing the material's thermodynamic stability. Additionally, compressive stress strengthens chemical bonds, endowing the lattice robustness to external perturbations such as photon energy or thermal fluctuations^{64,65}. These stabilizing effects contrast sharply with the tensile stress (+56 MPa) observed in the control film, which stretches lattice spacing and increases bond tension, making the lattice more prone to ruptures. After 20 h of illumination, the SDS-treated film transitions from an initial compressive stress (–55 MPa) to a slight tensile stress (+34 MPa), further suggesting that the flexible alkyl chains of SDS provide limited capacity to regulate initial stress and suppress light-induced stress accumulation. Although SDS treatment slows the rate of stress accumulation, the eventual emergence of

tensile stress expects to undermine long-term lattice stability by accelerating the ion migration and defect formation. The NTS-treated film retains compressive stress (–51 MPa) even after prolonged illumination. This exceptional stress resistance demonstrates the superior ability of NTS to mitigate light-induced stress, preserving lattice stability.

Under operational conditions, ion migration facilitates the formation of V_i and non-radiative recombination centers. By fitting the Arrhenius equation to temperature dependent conductivity results, the activation energies for ion migration (E_a^{ion}) were extracted, unveiling the interplay between stress modulation and ionic dynamics⁶⁶. As shown in Fig. 2e (fitted from Supplementary Fig. 15), the untreated control film exhibits the lowest activation energy ($E_a^{\text{ion}} = 395$ meV) for easy ion migration, which could be explained by the weakened Sn-I and Pb-I bonds under tensile stress. Contrarily, the SDS- and NTS-treated films manifest significantly higher activation energies for ion migration ($E_a^{\text{ion}} = 537$ meV and $E_a^{\text{ion}} = 694$ meV, respectively). This could be explained that compressive stress enhances bond strength, narrows lattice spacing, and increases the energy barrier for ion migration, effectively suppressing defect propagation and stabilizing the lattice. These findings show the pivotal role of stress modulation in controlling ionic migration and preserving the stability of perovskite materials.

To further investigate iodide ion migration in Sn-Pb perovskites under prolonged illumination, time-of-flight secondary ion mass spectrometry (TOF-SIMS) was employed to map the spatial distribution of iodide ions in both control and NTS-treated devices after 40 h of illumination (Fig. 2f, g). In the control film, significant iodide ion migration was observed, with iodide diffusing from the perovskite layer into the electron transport layer (ETL) and reaching the silver electrode, forming silver iodide through chemical reactions. These detrimental processes compromise charge extraction efficiency and undermine the long-term stability of the device. In contrast, the NTS-treated film demonstrates a localized iodide ion distribution, with ions confined to the perovskite layer even after extended illumination.

To quantitatively assess iodide ion migration and the release of iodine under prolonged illumination, perovskite films exposed to 10, 20, and 30 h of light were immersed in toluene, and UV-Vis (UV) absorption spectra in Supplementary Fig. 16 were recorded to track iodine-related peaks. Two characteristic absorption peaks are observed: the peak at ~500 nm corresponds to molecular iodine, likely formed by the oxidation of I^- at the film surface, while the peak at 300–350 nm is attributed to iodide ions or iodide-solvent complexes dissolved directly in toluene^{26,67}. In the control film, both peaks exhibit substantial intensity increments with elongating illumination time, reflecting severe iodide migration to the surface. At the surface, some iodide ions are oxidized to molecular iodine, contributing to the ~500 nm peak, while others dissolve directly into the toluene, leading to the 300–350 nm peak. This pronounced release of iodine evinces the instability of perovskite layer under light-induced stress, driven by lattice destabilization, Sn-I bond breaking, and the generation of structural defects. In comparison, the SDS-treated film demonstrates moderate suppression of iodine release, with less intensity increments for both peaks relative to the control. While the NTS-treated film exhibits minimal changes in both peaks, even after 30 h of illumination.

The process of I_2 oxidizing Sn^{2+} to Sn^{4+} was further analyzed by X-ray photoelectron spectroscopy (XPS), the relative amounts of Sn^{2+} and Sn^{4+} in the films before and after 20 h of illumination were summarized in Supplementary Fig. 17. It is seen that the proportion of Sn^{4+} in control film increases markedly from 13.35% to 24.22% after illumination. The significant oxidation of Sn^{2+} to Sn^{4+} disrupts the Sn-I bond network and introduces deep-level defect states into the film. While the SDS-treated film exhibits a moderate increase in Sn^{4+} content, from 6.55% to 9.65%, demonstrating its ability to partially inhibit Sn^{2+}

oxidation. Contrastingly, the NTS-treated film shows marginal increment of Sn^{4+} from 4.86% to 6.16% after 20 h of illumination. These results feature the superior stabilizing effect of NTS, which effectively limits iodine-mediated oxidation and helps maintain the structural integrity of Sn-Pb perovskites under prolonged light exposure.

XPS analysis of the Sn 3d spectra experimentally reveals the interactions between sulfonate groups in SDS and NTS and the Sn sites within the perovskite lattice (Supplementary Fig. 18). Specifically, the addition of SDS and NTS induce downward shift in the binding energies of Sn 3d_{5/2} from 495.7 eV to 495.6 eV and 495.4 eV, respectively, and Sn 3d_{3/2} from 487.3 eV to 487.2 eV and 487.0 eV. It indicates a strong coordination between sulfonate group and Sn, effectively stabilizing the chemical environment of Sn sites and reducing their activity. This stabilization enhances the Sn-I bond strength within the perovskite lattice, preventing bond rupture and suppressing the oxidation of Sn^{2+} to Sn^{4+} .

To elucidate the molecular-level interactions between sulfonate additives and the perovskite lattice, we first investigated hydrogen bonding with the organic A-site cations. Fourier transform infrared (FTIR) spectroscopy was employed to probe the N–H stretching region (3100–3500 cm^{-1}), as shown in Supplementary Fig. 19. The pristine FAI film exhibits a characteristic N–H vibrational mode at 3353.9 cm^{-1} . Upon additive incorporation, this peak red-shifts to 3349.7 (SDS), 3348.2 (SBS), 3345.8 (NSA), 3341.9 (NDS), and 3335.2 cm^{-1} (NTS), indicative of hydrogen bonding between the $-\text{NH}_3^+$ groups in FA^+ and sulfonate oxygen atoms. The degree of red-shift correlates with both the number and spatial accessibility of sulfonate groups, with NTS showing the largest shift due to its rigid trisulfonate structure. These hydrogen bonds serve to anchor the FA^+ cations within the lattice, restricting their vibrational and translational motion. This local confinement reduces dynamic disorder, stabilizes the neighboring iodide environment, and suppresses the formation of iodine vacancies (V_I), thereby improving overall structural coherence.

We further investigated the coordination interaction between sulfonate groups and the B-site metal cations by analyzing the 900–1250 cm^{-1} region of the FTIR spectra (Supplementary Fig. 20). Upon mixing each additive with PbI_2 and SnI_2 , both the asymmetric ($\nu_{\text{as}}(\text{S}=\text{O})$) and symmetric ($\nu_{\text{s}}(\text{S}=\text{O})$) stretching modes exhibit systematic red-shifts, confirming electron density transfer from sulfonate oxygens to the metal centers and the formation of coordination bonds.

The red-shifts are more pronounced in SnI_2 -containing systems than in those with PbI_2 , reflecting the higher Lewis acidity and coordinative unsaturation of Sn^{2+} . For instance, SDS-treated SnI_2 samples show marked downshifts in both $\nu_{\text{as}}(\text{S}=\text{O})$ and $\nu_{\text{s}}(\text{S}=\text{O})$, accompanied by the broadening or disappearance of the $\delta(\text{C}-\text{O}-\text{S})$ bending mode, suggesting strong Sn–O complexation. Similar patterns are observed for SBS. In contrast, NSA, bearing only one sulfonate group, induces minimal peak displacement, indicating weaker interaction. Notably, NDS and NTS exhibit the most significant spectral shifts and band broadening, especially in coordination with SnI_2 , consistent with stronger and possibly multidentate binding to Sn^{2+} . In some cases, peak merging or asymmetry arises due to overlap between $\nu_{\text{as}}(\text{S}=\text{O})$, $\nu_{\text{s}}(\text{S}=\text{O})$, and $\delta(\text{C}-\text{O}-\text{S})$ modes, but the overall red-shift trend remains consistent.

These observations provide compelling spectroscopic evidence for dual interaction modes of sulfonate additives—hydrogen bonding with A-site cations and coordination bonding with B-site Sn^{2+} and Pb^{2+} centers. Together, they contribute to lattice stabilization by reducing ionic motion, strengthening the inorganic framework, and mitigating light-induced degradation.

While the spectroscopic analyses above confirm that sulfonate additives interact with both A-site and B-site lattice species through hydrogen bonding and coordination, the functional impact of these interactions depends critically on their spatial localization. Grain boundaries are structurally disordered, defect-prone, and stress-

concentrated regions, thus representing key sites of lattice instability under illumination^{68–70}.

To directly examine the spatial distribution of additives within perovskite films, we performed scanning transmission electron microscopy (STEM) combined with energy-dispersive X-ray spectroscopy (EDS) line-scan analysis, focusing on grain boundary regions. As shown in Supplementary Fig. 21, the yellow dashed lines delineate the boundaries between adjacent crystalline grains. In the control film, sulfur signals originating from sulfonate groups are nearly undetectable across the scanned regions. In contrast, all sulfonate-treated films exhibit clear and localized sulfur enrichment at the grain boundaries, as revealed by the EDS profiles along the red line scan paths. This spatially confined sulfur signal provides direct evidence that sulfonate-based additives preferentially accumulate at grain interfaces, which are known to host high defect densities, residual strain, and serve as initiation sites for light-induced degradation. These findings support a selective binding mechanism, in which sulfonic acid groups coordinate with Sn^{2+} and Pb^{2+} ions at grain surfaces.

The surface potential distribution of perovskite films and its correlation with electronic properties were then studied by kelvin probe force microscopy (KPFM) measurements (Supplementary Fig. 22). Before illumination, the control film exhibits a broad potential distribution centered around -20 mV, indicating considerable non-uniformity and a high surface defect density. The NTS-treated film displays a much narrower distribution centered at 416 mV, reflecting improved surface potential uniformity. The more positive potential in the NTS-treated film suggests enhanced n-type characteristics, facilitating electron transport across the surface and improving charge extraction. After 40 h of illumination, high work function regions, corresponding to the formation of degradation products such as PbI_2 emergence in the control film, which could be attributed to the light-induced iodide migration and structural instability⁷¹. While the NTS-treated film maintains a uniform surface potential distribution, indicative of a suppressed decomposition.

Notably, the enhanced n-type character of NTS-treated films can be attributed to the effective passivation of surface and interfacial defects, particularly undercoordinated metal ions and halide vacancies, by the trisulfonate groups. These interactions reduce electron trapping near the surface and suppress non-radiative recombination. This mechanism is further supported by density functional theory (DFT) calculations. As shown in Supplementary Fig. 23, the adsorption energy of NTS on a pristine Sn–Pb perovskite surface is -6.87 eV, significantly more negative than that of SDS (-2.28 eV), indicating much stronger binding affinity. This enhanced binding is attributed to the rigid aromatic backbone and multidentate sulfonate architecture of NTS, which enable stable multi-point anchoring to the perovskite lattice. Further analysis, as shown in Fig. 3a, compares the adsorption energies of NTS and SDS on intrinsic defects, classified as donor defects (V_I , V_{Sn}) and acceptor defects (V_{FA} , Sn_I , I_{Sn}). In all cases, NTS exhibits substantially more negative adsorption energies than SDS, reflecting stronger interactions with both donor- and acceptor-type defects. Supplementary Figs. 24 and 25 show the specific adsorption models of three representative intrinsic defects of SDS and NTS, respectively: V_I , Sn_I and I_{Sn} . The differential charge density plots reveal significant electron redistribution at the interface between NTS and the surface, indicating stable chemical coupling and defect passivation. In contrast, SDS exhibits weak local interactions and minimal charge transfer, which is consistent with its lower passivation efficiency. Importantly, the strong surface binding force of NTS can not only neutralize existing traps, but also increase the formation energy of defect sites, thereby kinetically suppressing the generation of new defects under illumination. This dual function helps minimize non-radiative recombination, enhance carrier mobility, and improve the long-term optoelectronic performance and structural stability of Sn–Pb perovskite films. The density of states (DOS) and projected density

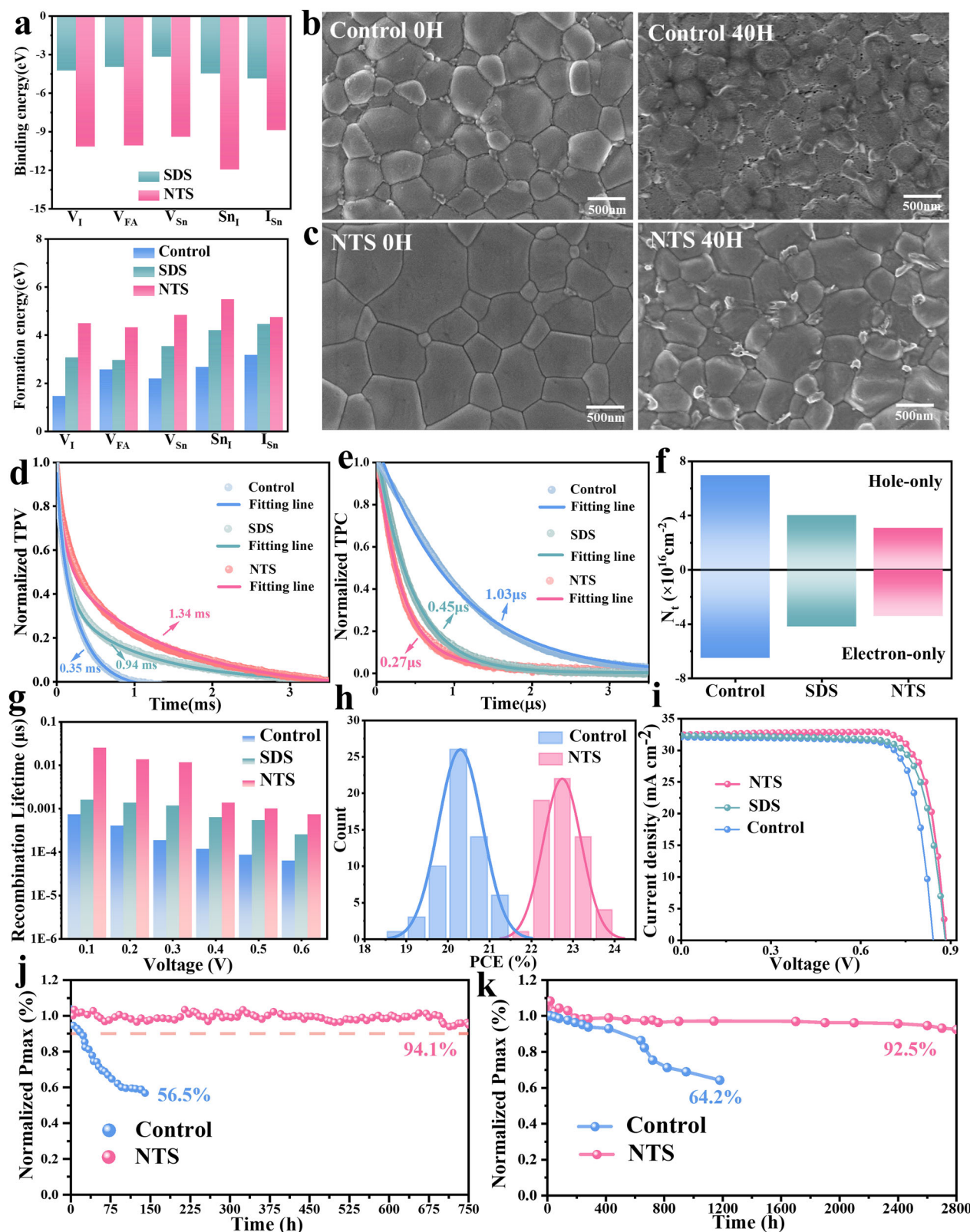


Fig. 3 | Performance and stability of NBG single-junction PSCs. **a** Binding energies (E_b) of SDS and NTS with Sn, FA and I vacancy defects (V_{Sn} , V_{FA} and V_I), I interstitial defects (I_i) and I substituted at the Sn site (I_{Sn}) on the perovskite surface and their defect formation energies (E_f). Scanning electron microscopy (SEM) images of the perovskite film without illumination and after illumination for 40 h pristine perovskite film (**b**) and NTS perovskite film (**c**). Transient photovoltage (TPV) decay curves (**d**). Transient photocurrent (TPC) decay curves (**e**). **f** Trap density (N_t) values for control, SDS-treated, and NTS-treated Sn-Pb perovskite films

determined using space-charge-limited current (SCLC) analysis. **g** Recombination lifetime of devices under different biases derived from the Nyquist plots (Supplementary Fig. 39). The statistical PCE of Sn-Pb PSCs with different treatments (**h**). **j**-**v** curves (**i**) of the best performing devices under control and modified with NTS. **j** MPP tracking of control devices and devices with NTS under 1 sun illumination in the N_2 environment. **k** Long-term stability test of control devices and devices with NTS Sn-Pb PSCs stored in an N_2 -filled glovebox.

of states (PDOS) analyses further corroborate the electronic-level defect passivation mechanism of NTS. As shown in Supplementary Fig. 26, intrinsic defects such as V_i , Sn_i , and I_{Sn} introduce mid-gap states or shallow donor levels that act as non-radiative recombination centers. Upon NTS binding, these defect-induced states are either significantly suppressed or shifted toward the band edges, effectively mitigating their electronic activity. Notably, the partial DOS of Sn atoms coordinated with sulfonate oxygens reveals a redistribution of electronic density and reduction of deep-level defect states. This suppression of mid-gap states is particularly evident in V_i and Sn_i configurations, where the DOS near the Fermi level is markedly reduced after NTS treatment. These results highlight that NTS not only passivates structural defects through strong surface anchoring, but also electronically deactivates trap states by modulating the local density of states, thereby preserving charge transport and enhancing device stability under illumination.

To visually consolidate these experimental and theoretical insights, we present a schematic illustration of the proposed sulfonate-mediated stabilization mechanism (Supplementary Fig. 27). In this model, sulfonate additives are shown to selectively anchor at grain boundaries, where the molecular architecture of NTS enables spatially localized, multipoint coordination with Sn^{2+} ions. In parallel, hydrogen bonding with A-site cations further enhances interfacial binding stability. This dual-interaction framework reflects the combined advantages of multidentate geometry and interfacial selectivity, both of which are essential for effective defect passivation, suppression of ion migration, and lattice strain relaxation. By integrating spatial targeting with chemical functionality, this model captures the core design principles underpinning the bond-centric and lattice-intrinsic stabilization achieved in this work.

Scanning electron microscopy (SEM) images reveal substantial morphological differences between the SDS-treated and NTS-treated films before and after prolonged illumination. Prior to illumination, both SDS- and NTS-treated films exhibit enlarged grains compared to the control film, with average grain sizes of 783.5 nm and 892.2 nm, respectively (Supplementary Figs. 28, 29 and Fig. 3b, c). This indicates enhanced crystallinity and fewer grain boundary defects, which are crucial for suppressing ionic migration, reducing non-radiative recombination, and improving charge transport. Notably, the NTS-treated film demonstrates a uniform surface morphology, free from residual lead iodide, in stark contrast to the control film, which shows PbI_2 segregation at grain boundaries, a feature often associated with accelerated degradation¹². After 20 h of illumination, the SDS-treated film exhibits moderate surface roughening and degradation at grain boundaries as seen in Supplementary Fig. 30. The flexible alkyl chains in SDS partially stabilize the grain boundaries, delaying the onset of significant void formation. However, after 40 h, pronounced voids and cracks are observed, indicating that SDS offers limited protection under prolonged light-induced stress and cannot fully prevent structural deterioration. The NTS-treated film demonstrates exceptional morphological stability upon 40 h of illumination. The grains remain intact, and the surface retains a smooth, compact morphology free from voids or amorphization.

X-ray diffraction (XRD) analysis was carried out to assess the effect of additives on the crystallinity of Sn-Pb perovskite films (Supplementary Fig. 31). The results show that the (100) diffraction peak intensity increases and the FWHM significantly narrows following SDS and NTS treatment, indicating enhanced crystallinity⁷². Moreover, a diffraction peak at 12.7° , corresponding to PbI_2 , was observed in the control film. This peak, consistent with the PbI_2 aggregates seen in SEM images, was absent in the SDS- and NTS-treated films, suggesting effective suppression of PbI_2 formation by the additives.

TOF-SIMS depth profiles of the control film (Supplementary Fig. 32) show that Sn is predominantly concentrated near the top surface, while Pb is localized toward the bottom, creating a

pronounced compositional gradient. This uneven distribution arises from differences in the solubility and crystallization kinetics of Sn- and Pb-based perovskite phases⁷³. The resulting Pb/Sn gradient induces lattice strain and structural distortions, which exacerbate photo-degradation and compromise device stability. Differently, the NTS-treated film exhibits a highly uniform Pb and Sn distribution across the entire film. The observed homogeneity in the NTS-treated film is attributed to the trisulfonate groups in NTS, which strongly coordinate with Pb^{2+} ions, stabilizing Pb intermediates and lowering the nucleation energy barrier. This selective promotion of Pb crystallization aligns the growth kinetics of Pb- and Sn-based phases, eliminating the disparities of solubility and crystallization dynamics as seen in the control film. The uniform Pb and Sn distribution contributes to reducing lattice strain and ensuring consistent electronic properties across the film.

Grazing incident wide angle X-ray scattering (GIWAXS) analysis provides insights into the crystallographic properties of the (100) plane (Supplementary Fig. 33). In the control film, the (100) peak splits into multiple sub-peaks at grazing angles of 0.1° , 0.2° , and 0.4° , indicating the presence of significant lattice strain and structural heterogeneity along the vertical direction. Additionally, the (100) peak shifts to lower angles with increasing grazing incidence angle, suggesting a compositional gradient with surface regions enriched in Sn, consistent with TOF-SIMS results. In contrast, the NTS-treated film exhibits a single sharp (100) peak consistently at 14.12° across all grazing incidence angles (0.1° – 0.8°), suggesting a uniform lattice structure and the absence of strain or compositional gradients⁷⁴.

The PL spectra of the control, SDS-treated, and NTS-treated perovskite films are presented in Supplementary Fig. 34. Among these samples, the NTS-treated film exhibits the highest PL intensity, followed by the SDS-treated film, with control film showing the lowest intensity. This trend manifests the superior defect passivation and suppressed nonradiative recombination in the NTS-treated film, consistent with its higher defect formation energy and improved structural uniformity observed in previous analyses. Moreover, the pronounced blue shift in the PL peak position for NTS-treated film, further supports the reduction in defect states. To complement these findings, time-resolved photoluminescence (TRPL) measurements were conducted (Supplementary Fig. 35). The NTS-treated film demonstrates the longest carrier lifetime ($10.9 \mu s$), exceeding the SDS-treated film ($9.8 \mu s$) and the control film ($5.4 \mu s$), reflecting reduced non-radiative recombination.

To directly evaluate the oxidation resistance of Sn^{2+} in precursor solutions, we compared three formulations: control (no additive), SDS-treated, and NTS-treated. All freshly prepared solutions initially exhibited a bright yellow color, characteristic of Sn^{2+} species (Supplementary Fig. 36). Upon exposure to ambient air, the control solution rapidly darkened within 1 min and turned reddish brown after 5 min, indicating substantial oxidation of Sn^{2+} to Sn^{4+} . The SDS-treated solution showed moderate discoloration, suggesting limited suppression of this oxidative process. In stark contrast, the NTS-containing solution retained its yellow color even after 5 min of air exposure, clearly demonstrating markedly improved resistance to Sn^{2+} oxidation. This enhanced stability is attributed to the strong coordination between the sulfonate groups of NTS and Sn^{2+} centers, which stabilizes the Sn oxidation state and reinforces Sn–I bonds. As supported by COHP and Raman analyses, this interaction reduces the likelihood of Sn–I bond cleavage under oxidative environments, thereby mitigating both light- and oxygen-induced degradation pathways at the molecular level.

Performance and stability of NBG single-junction PSCs

Charge extraction kinetics and carrier lifetimes under operational conditions were studied through transient photovoltage (TPV) and transient photocurrent (TPC) measurements. TPC analysis illustrated

in Fig. 3d reveals that the NTS-treated device exhibits the fastest charge extraction dynamics, with a decay time of 0.27 μ s, outperforming the SDS-treated (0.45 μ s) and control (1.03 μ s) devices. The faster decay indicates facilitated charge extraction from the perovskite layer to adjacent transport layers, attributed to the uniform grain structure and superior interfacial quality with NTS treatment. These structural improvements reduce energy barriers for charge transfer and minimize carrier accumulation at grain boundaries. TPV analysis (Fig. 3e) further emphasizes the role of defect passivation and structural optimization in suppressing carrier recombination⁷⁵. The NTS-treated device demonstrates the longest carrier lifetime of 1.34 ms, substantially exceeding that of the SDS-treated (0.94 ms) and control (0.35 ms) devices. The slower decay observed in the NTS-treated device signifies reduced non-radiative recombination rates and a lower density of trap states.

Space-charge-limited current (SCLC) measurements were conducted to quantitatively determine the trap density (N_t) in perovskite films using hole-only and electron-only devices (Supplementary Fig. 37 and Fig. 3f). The trap-filled limit voltage (V_{TFL}) and corresponding N_t values were extracted and summarized in Supplementary Tables 4 and 5. Following SDS and NTS treatment, the V_{TFL} values for hole-only devices decrease from 0.45 V (control) to 0.26 V and 0.20 V, respectively, while for electron-only device, the V_{TFL} decrease from 0.42 V to 0.27 V and 0.22 V. Moreover, the N_t values for the control film, initially $6.96 \times 10^{16} \text{ cm}^{-3}$ (hole-only) and $6.50 \times 10^{16} \text{ cm}^{-3}$ (electron-only), reduce to $4.02 \times 10^{16} \text{ cm}^{-3}$ and $4.18 \times 10^{16} \text{ cm}^{-3}$ for SDS-treated films, and further to $3.09 \times 10^{16} \text{ cm}^{-3}$ and $3.40 \times 10^{16} \text{ cm}^{-3}$ for NTS-treated films. These reductions in V_{TFL} and N_t values demonstrate the ability of SDS and NTS to inhibit iodide ion migration, enhance charge extraction, and suppress non-radiative recombination.

Mott-Schottky (MS) analysis was conducted to assess the built-in potential (V_{bi}) and its relationship with charge transport properties in PSCs (Supplementary Fig. 38). The control device exhibits the lowest V_{bi} of 0.56 V. In contrast, the SDS-treated device shows an improved V_{bi} of 0.69 V. Notably, the NTS-treated device achieves the highest V_{bi} of 0.73 V, reflecting superior interfacial energy alignment and a stronger internal electric field. These findings align with the improved carrier dynamics observed in TPV and TPC measurements.

To investigate charge recombination dynamics at the device level, electrochemical impedance spectroscopy (EIS) measurements were performed on PSCs over an external voltage range of 0.1–0.6 V. Depicted in Supplementary Fig. 39, the recombination resistance (R_{rec}) of Sn-Pb perovskite devices modified with NTS and SDS exhibit a significant increment compared to control devices at the same voltage. A larger R_{rec} value reflects the suppression of charge recombination processes. Additionally, the carrier recombination lifetime, extracted and summarized in Fig. 3g, demonstrates an extended carrier lifetime for the NTS-treated device²⁷.

Building on the enhanced film properties achieved with SDS and NTS incorporation, single-junction Sn-Pb PSCs were fabricated using an inverted p-i-n structure consisting of indium tin oxide (ITO)/poly(3,4-ethylenedioxythiophene): polystyrene sulfonate (PEDOT:PSS)/NBG perovskite/ C_{60} /bathocuproine (BCP)/Ag. The optimal additive concentrations were identified as 0.8 mg/mL for SDS and 0.5 mg/mL for NTS (Supplementary Fig. 40). The detailed photovoltaic parameters, including open-circuit voltage (V_{OC}), short-circuit current density (J_{SC}), fill factor (FF), and PCE for the control and NTS-treated devices, are summarized in Supplementary Table 6, with the corresponding J-V curves displayed in Fig. 3i. Experiments using Na^+ , K^+ , and Li^+ salts of NTS reveal negligible variation in device performance, confirming that the observed effect originates from the sulfonate anion rather than the counter cation (Supplementary Fig. 41). Upon NTS treatment, the photovoltaic performance of the PSCs exhibits marked improvements. The V_{OC} increasing from 0.84 V to 0.88 V could be attributed to the reduced non-radiative recombination enabled by

effective defect suppression. Simultaneously, the J_{SC} rising from 32.1 mA/cm² to 32.5 mA/cm² could be primarily due to improved charge carrier extraction in NTS-modified perovskite film. UV-vis absorption spectra (Supplementary Fig. 42) further reveal increased absorption intensity in the visible region upon NTS incorporation, contributing to improved photocurrent. Importantly, Tauc plot analysis (Supplementary Fig. 43) confirms that the optical bandgap (~1.26 eV) remains unchanged, indicating that additive incorporation does not alter the intrinsic band structure. External quantum efficiency (EQE) measurements corroborated the J_{SC} values of NTS-treated PSCs (Supplementary Fig. 44). These combined advancements culminate in a PCE of 23.2% for the champion device, significantly outperforming the control PSC of 21.3%.

In addition to the superior device efficiency, NTS treatment also brings substantial improvements in the reproducibility and stability of the devices. The average PCE of 60 single-junction NBG PSCs also improves to 22.8% with NTS treatment, compared to 20.3% for the control devices (Fig. 3h). During 300 seconds of stabilized power output (SPO) testing, NTS-treated device maintains a stable PCE of 23.1% (Supplementary Fig. 45). Operational stability under MPP tracking at continuous 1-sun illumination shows that the NTS-treated device retains 94.1% of its initial PCE after 750 h, in stark contrast to the control device, which drops to 56.5% after 150 h (Fig. 3j). By addressing key degradation mechanisms, including ion migration, lattice strain, and structural instability, NTS significantly stabilizes the lattice framework of Sn-Pb PSCs. These optimizations synergistically ensure that NTS-treated devices retain high performance and long-term durability under operational conditions. Additionally, long-term shelf storage stability demonstrates that the encapsulated NTS-treated device preserved 92.5% of its initial PCE after 2800 h, whereas the control device declines to 64.2% after 1200 h (Fig. 3k).

To disentangle the contributions of grain size and chemical coordination, we performed a comparative analysis using two NTS incorporation strategies: interface-only modification and full bulk incorporation. As shown in Supplementary Figs. 46–48, both treatments result in significant improvements in efficiency and operational stability relative to the control. However, SEM analysis reveals that only bulk incorporation induces substantial grain growth, while interface-modified films maintain a similar average grain size (~691.2 nm, Supplementary Fig. 47) to the control (~627.8 nm, Supplementary Fig. 29). Despite this morphological similarity, interface-only devices still exhibit excellent stability, retaining 90.0% of their initial PCE after 510 h of continuous illumination (Supplementary Fig. 48), indicating that morphological changes are not a prerequisite for performance enhancement. These results confirm that improved Sn-I bonding, rather than grain enlargement, plays the dominant role in enhancing stability.

Performance and stability of 2T PTSCs

The optimized NBG perovskite is then employed as the bottom sub-cell in PTSCs. The tandem devices incorporate a 1.78 eV WBG perovskite as the top sub-cell and adopt a monolithic 2T architecture with the following layer sequence: ITO/ NiO_x /Me-4PACz/WBG-PSCs/ C_{60} /SnO₂/Au/PEDOT:PSS/NBG-PSCs/ C_{60} /BCP/Ag (Supplementary Fig. 49). The integration of the two sub-cells is confirmed through cross-sectional SEM image (Fig. 4a). The J-V curves of the used WBG-PSCs are shown in Supplementary Fig. 50 with a PCE of 19.9% and the detailed parameters are shown in Supplementary Table 7. Ultimately, the champion PTSC achieves an outstanding PCE of 29.6%, with V_{OC} of 2.17 V, J_{SC} of 16.45 mA/cm², and FF of 82.8% (Fig. 4b and Supplementary Table 8). Meanwhile, a reputable third-party organization gives certified PCE of 29.2% (Supplementary Fig. 51), one of the highest efficiencies reported so far (Supplementary Table 9). The corresponding tandem cell also exhibits a stabilized PCE of up to 29.6% (Supplementary Fig. 52). The EQE spectra of the WBG and NBG sub-cells

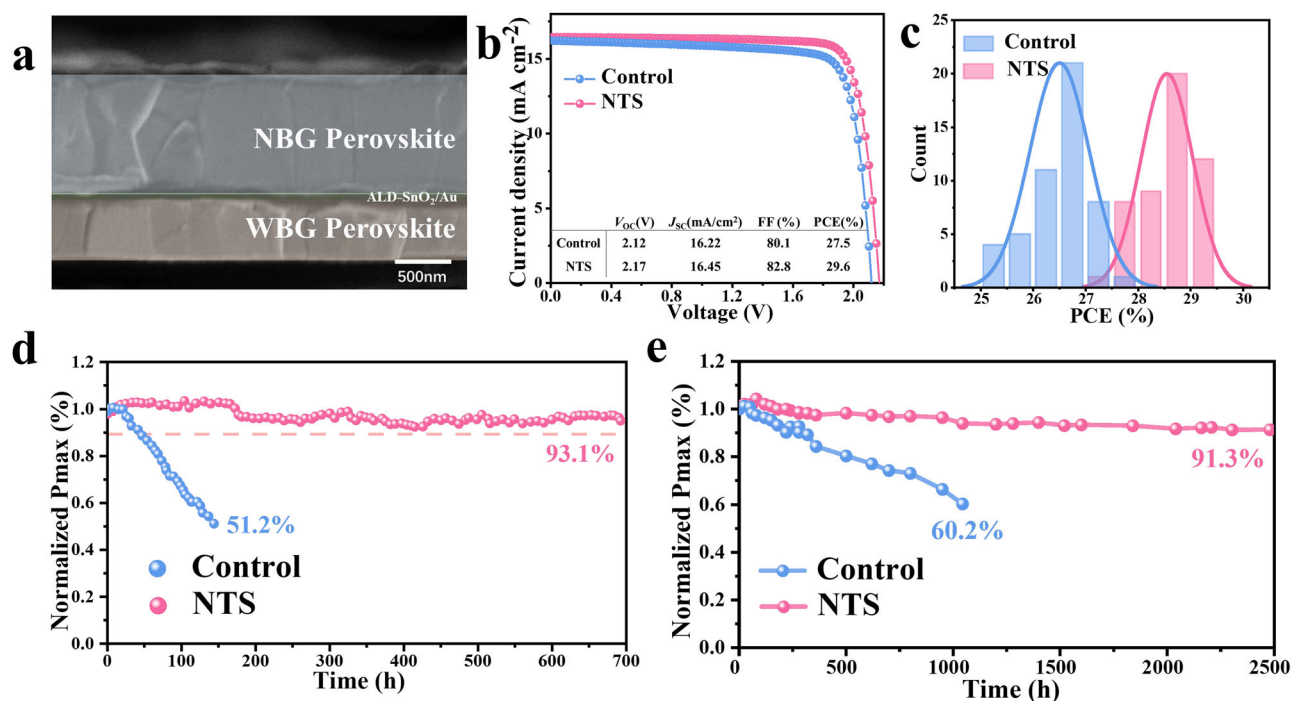


Fig. 4 | Performance and stability of 2T PTSCs. **a** Cross-section SEM image of PTSCs with NTS modification. **b** J-V curves of the best-performing PTSCs. **c** Histogram of PCEs for 50 PTSCs. **d** MPP tracking of control device and device with

NTS under 1 sun illumination in the N₂ environment. **e** Long-term stability test of control device and device with NTS PTSCs stored in a N₂-filled glovebox.

(Supplementary Fig. 53) are consistent with the integrated J_{sc} values derived from J-V measurements, affirming the accuracy and performance of the tandem design. Reproducibility is further evaluated by fabricating 50 tandem devices, demonstrating consistent performance across the batch and confirming the reliability of the optimized structure (Fig. 4c).

NTS incorporation significantly improves both the operational and storage stability of tandem devices. The encapsulated PTSC retains 93.1% of its initial PCE after 700 h of continuous operation under MPP tracking, in stark contrast to the rapid degradation observed in the control device (Fig. 4d). Furthermore, during extended storage in a nitrogen-filled glove box, the control device's PCE declines to 60.2% of its initial value after 1100 h, whereas the NTS-treated device maintains 91.3% of its original PCE even after 2500 h (Fig. 4e). These findings highlight the critical role of NTS in reinforcing lattice stability and mitigating performance losses, thereby enabling high-efficiency and durable tandem solar cells.

Discussion

This study presents a robust strategy to address critical challenges in Sn-Pb NBG perovskites, specifically lattice instability, strain heterogeneity and halide migration through the incorporation of sulfonate-based molecular additives. Among these, NTS with the high molecular rigidity exhibits the most efficacy in strengthening Sn-I bonds, suppressing dynamic lattice distortions, and alleviating localized stress accumulation, thereby stabilizing the Sn-Pb perovskite lattice. By reducing the strain heterogeneity and compositional gradients, NTS promotes uniform lattice alignment and preserves structural integrity under operational conditions. As a result, the optimized Sn-Pb NBG perovskite achieves a PCE of 23.2%, with 94.1% of the initial efficiency retained after 750 h of MPP tracking. When incorporated into 2T PTSCs, this system attains an impressive PCE of 29.6% (certified PCE of 29.2%), maintaining 93.1% of its initial efficiency after 700 h of continuous operation. This work establishes lattice stabilization as a critical pathway to overcoming degradation in Sn-Pb perovskites,

offering an innovative strategy to achieve exceptional structural and operational stability in tandem devices. These advancements provide a strong foundation for the commercial deployment of next-generation photovoltaic technologies.

Methods

Materials

All materials were utilized as received without any further purification. FAI, 99.99%, methylammonium chloride (MAI 99.99%), PbI₂ (99.9%), lead chloride (PbCl₂ 99.9%), SnI₂ (99.9%), Nickel oxide (NiO_x) and patterned ITO substrates were purchased from Advanced Election Technology CO, Ltd. Methylammonium iodide (MAI), cesium iodide (CsI), Pb bromide (PbBr₂), 1,3-propane-diammonium iodide (PDAl₂) and ethanediamine dihydroiodide (EDAl₂) were supplied from Xi'an Polymer Light Technology Corporation. Isopropanol (IPA, 99.9%), chlorobenzene (CB, 99.9%), diethyl ether (DE), N, N-dimethyl formamide (DMF, 99.8%), and dimethyl sulfoxide (DMSO, 99.7%) were obtained from Beijing J&K Scientific Ltd. SDS (98%), SBS (98%), NSA (98%), NTS (98%) and NTS (98%) were procured from Aladdin. Sn (II) fluorine (SnF₂, 99%) and ammonium thiocyanate (NH₄SCN, 99.9%) and Pb (II) thiocyanate (Pb (SCN)₂, 99.9%) were purchased from Sigma-Aldrich. PEDOT: PSS (CLEVIO P VP AI 4083) was purchased from Heraeus.

NBG FA_{0.6}MA_{0.3}Cs_{0.1}Pb_{0.5}Sn_{0.5}I₃ perovskite solution preparation

To prepare the 2.0 M perovskite precursor solution, dissolve the following amounts of each compound in 1 mL of a mixed solvent of DMF and DMSO (3:1, v/v): 459.54 mg of PbI₂, 372.79 mg of SnI₂, 206.46 mg of FAI, 95.27 mg of MAI, 51.91 mg of CsI, 15.65 mg of SnF₂, and 2.86 mg of NH₄SCN. For additive-treated samples, sulfonate-based molecular additives were directly added into the precursor solution at the following optimized concentrations: 0.8 mg/mL for SDS, 0.7 mg/mL for SBS and NSA, 0.6 mg/mL for NDS, and 0.5 mg/mL for NTS. Stir the mixture thoroughly until all components are completely dissolved.

Finally, filter the solution through a 0.22 μm polytetrafluoroethylene (PTFE) membrane to remove any undissolved particles before using it to prepare perovskite films.

WBG $\text{FA}_{0.8}\text{Cs}_{0.2}\text{PbI}_{1.8}\text{Br}_{1.2}$ perovskite solution preparation

Dissolve 212.06 mg of PbI_2 , 271.58 mg of PbBr_2 , 165.1 mg of FAI , 6.67 mg of PbCl_2 , 62.4 mg of CsI , 1.62 mg of MACl , and 4.8 mg of $\text{Pb}(\text{SCN})_2$ in a 1 mL mixed solvent of DMF and DMSO, with a volume ratio of 4:1 (DMF:DMSO).

NBG Sn-Pb PSCs fabrication

The patterned ITO substrates were first ultrasonically cleaned sequentially with detergent, deionized water, acetone, and isopropanol, with each step lasting 30 min. The substrates were then dried using N_2 gas and treated with plasma for 5 min. Subsequently, the cleaned ITO substrates were spin-coated with a PEDOT: PSS solution at 4000 rpm for 30 s, followed by annealing at 150 $^\circ\text{C}$ for 15 min in air. The films were then transferred to an N_2 -filled glovebox for further processing. The NBG precursor solution was spin-coated onto the substrates using a two-step process: an initial spin at 1000 rpm for 10 s, followed by a second spin at 4000 rpm for 30 s. During the second spin, CB as the antisolvent was dripped onto the film at 30 s. The coated films were then annealed at 100 $^\circ\text{C}$ for 10 min inside the glovebox. Subsequently, the EDAI_2 layer precursor solution (1.0 mg mL^{-1} in IPA) was spin-coated at 4000 rpm for 20 s, followed by annealing at 100 $^\circ\text{C}$ for 1 min. Finally, 25 nm of C_{60} , 6 nm of BCP, and 100 nm of Ag were deposited sequentially via thermal evaporation.

All-perovskite tandem solar cell fabrication

NiOx nanocrystal layers (10 mg mL^{-1} in H_2O) were spin-coated onto ITO substrates at 1500 rpm for 30 s and subsequently annealed at 150 $^\circ\text{C}$ for 30 min in air. After cooling, the substrates were promptly transferred to an N_2 -filled glovebox. Next, self-assembled monolayers of Me-4PACz (0.3 mg mL^{-1} in ethanol) were spin-coated onto the ITO substrates at 3000 rpm for 30 s, followed by heating at 100 $^\circ\text{C}$ for 10 min. The WBG perovskite films were then deposited using a two-step spin-coating procedure: an initial spin at 5000 rpm for 2 s and a second spin at 4000 rpm for 60 s. During the second step, diethyl ether (DE) was dropped onto the spinning substrate at 25 s. The substrates were then transferred onto a hotplate and annealed at 100 $^\circ\text{C}$ for 10 min. After the substrates were cooled, post-treatments with PDAI_2 were conducted via spin-coating a solution of 2 mg/mL PDAI_2 in IPA at 4000 rpm for 30 s, followed by annealing at 100 $^\circ\text{C}$ for 5 min. After cooling to room temperature, the substrates were transferred to an evaporation system for the deposition of a 25 nm C_{60} layer. ALD SnO_2 layers with a thickness of 20 nm were then deposited onto the WBG perovskite films, followed by the deposition of a 1.0 nm Au layer via thermal evaporation. PEDOT: PSS layers were subsequently spin-coated on top of the front cells at 4000 rpm for 30 s and annealed at 120 $^\circ\text{C}$ for 20 min in air. Finally, the substrates were transferred back to the N_2 -filled glovebox for the fabrication of the NBG films, which were deposited and processed following the procedure described above.

DFT calculations

The defect formation energy and adsorption energy were calculated using DFT methods implemented in the Vienna Ab initio Simulation Package (VASP). The Perdew–Burke–Ernzerhof (PBE) functional was employed to simulate electron exchange–correlation interactions, while the projector augmented wave (PAW) method was used to describe electron–ion–nucleus interactions. Long-range van der Waals interactions in the perovskite system were accounted for using the Grimme DFT-D3 approach with Becke–Johnson damping. Geometry optimizations were performed using a Γ -centered $2 \times 2 \times 2$ Monkhorst–Pack k-point mesh and a plane wave energy cutoff of 400 eV.

Convergence was achieved when the energy difference between all ions was smaller than 10^{-4} eV. Based on the optimized perovskite surface model, a defect model was constructed, and SDS or NTS molecules were adsorbed on the surface to investigate the influence of adsorbed organic ions on surface defects.

For AIMD simulations, first-principles DFT calculations were performed with the PAW method using the PBE functional within the generalized gradient approximation (GGA). A plane wave energy cutoff of 500 eV was used, and the Brillouin zone was sampled with a $1 \times 1 \times 1$ k-point grid. Geometry relaxation was conducted until atomic forces were below 0.03 eV/ \AA , and self-consistent calculations were converged to an energy threshold of 10^{-5} eV. To avoid interactions between periodic structures, a vacuum layer of 15 \AA was introduced along the z-direction. AIMD simulations were performed for 10 ps within the canonical (NVT) ensemble at 300 K using a Nosé–Hoover thermostat with a time step of 1 fs. The calculation of the BAV and DI was based on reported literature methods.

Device characterization

The performance characterization of the devices was conducted using a Newport Oriel Sol3A 450 W solar simulator under AM 1.5 G illumination. This setup was used to measure J–V curves and SPO, as well as to characterize conductivity and perform SCLC analysis under dark conditions. The tested solar cell area was 0.116 cm^2 , with an aperture shading mask applied to define an effective area of 0.08 cm^2 . The EQE spectra of the devices were measured using a solar cell quantum efficiency test system (Elli Technology, Taiwan). EQE measurements were performed by applying external voltage/current sources to the PSCs using an REPS measurement instrument (Enlitech). The MS and EIS analyses were conducted with a Chenhua CHI760E electrochemical workstation. Operational stability tests for the NBG and tandem solar cells were carried out under MPP conditions in an N_2 environment, illuminated by an AM 1.5 xenon lamp (100 mW/cm^2 , without UV filter). TOF-SIMS analysis was performed using a dual-beam technique. Primary ion bombardment was conducted with Bismuth (Bi^{3+}) ions at an energy of 30 keV and a current of 45 nA, while secondary ion detection utilized Cesium (Cs^+) ions at an energy of 1 keV and a current of 80 nA. The secondary ion beam was aligned at 45 $^\circ$ to the primary ion path. Additionally, a flood gun was employed to neutralize surface charges, ensuring high mass resolution and accurate ion yield.

Film characterization

The FTIR spectroscopy was detected by FTIR-8400S (Shimadzu). XPS was measured by Kratos axial super dald. For the calibration of XPS data, the instrument was calibrated using the binding energy positions of Au 4f_{7/2}, Ag 3d_{5/2}, and Cu 2p_{3/2} spectral peaks, respectively. The calibration error of instrument is 0.10 eV, and the binding energy error during the test is within 0.1 eV. SEM images were obtained by scanning electron microscope (verios G4 UC) (Rimono Scientific Company, USA) at 2 kV. The IDPC-TEM images were captured using Titan-G2 (60–300) and JEOL ARM-300 spherical aberration-corrected transmission electron microscopes. The steady PL spectra were recorded on the Horiba jobin Yvon ffluorolog-3 spectrofluorometer system and PL mapping was measured by HORIBA HR Evolution. TRPL was analyzed by the FLS 980 fluorescence spectrometer equipped with a 532 nm excitation. The KPFM images were captured by Dimension ICON SPM (Dimension Icon, German). Chi 660e electrochemical measurement workstation (Chengdu equipment company, Shanghai, China) was used for SCLC analysis under dark conditions. GIXRD were characterized using a Rigaku SmartLab five-axis X-ray diffractometer at 45 kV and 200 mA, equipped with Cu K α radiation ($\lambda = 1.54050 \text{ \AA}$), parallel beam optics and a secondary graphite monochromator. GIWAXS measurements were measured by the XEUS SAXS/WAXS equipment.

Reporting summary

Further information on research design is available in the Nature Portfolio Reporting Summary linked to this article.

Data availability

The data generated in this study are provided in the Supplementary Information and Source Data file. Additional datasets that support the findings of this study are available from the corresponding author upon request. Source data are provided with this paper.

References

- Li, Q. et al. Harmonizing the bilateral bond strength of the interfacial molecule in perovskite solar cells. *Nat. Energy* <https://doi.org/10.1038/s41560-024-01642-3> (2024).
- Li, S. et al. Coherent growth of high-Miller-index facets enhances perovskite solar cells. *Nature* **635**, 874–881 (2024).
- Liu, S. et al. Buried interface molecular hybrid for inverted perovskite solar cells. *Nature* **632**, 536–542 (2024).
- Wu, J. et al. Inverse design workflow discovers hole-transport materials tailored for perovskite solar cells. *Science* **386**, 1256–1264 (2024).
- Li, C. et al. Diamine chelates for increased stability in mixed Sn–Pb and all-perovskite tandem solar cells. *Nat. Energy* **9**, 1388–1396 (2024).
- Zhou, J. et al. Mixed tin-lead perovskites with balanced crystallization and oxidation barrier for all-perovskite tandem solar cells. *Nat. Commun.* **15**, 2324 (2024).
- Duan, C. et al. Scalable fabrication of wide-bandgap perovskites using green solvents for tandem solar cells. *Nat. Energy* <https://doi.org/10.1038/s41560-024-01672-x> (2024).
- Pan, Y. et al. Surface chemical polishing and passivation minimize non-radiative recombination for all-perovskite tandem solar cells. *Nat. Commun.* **15**, 7335 (2024).
- Lim, J., Park, N.-G., Il Seok, S. & Saliba, M. All-perovskite tandem solar cells: from fundamentals to technological progress. *Energy Environ. Sci.* **17**, 4390–4425 (2024).
- Hu, S. et al. Steering perovskite precursor solutions for multi-junction photovoltaics. *Nature* <https://doi.org/10.1038/s41586-024-08546-y> (2024).
- Liu, Z. et al. All-perovskite tandem solar cells achieving >29% efficiency with improved (100) orientation in wide-bandgap perovskites. *Nat. Mater.* <https://doi.org/10.1038/s41563-024-02073-x> (2025).
- Zhou, S. et al. Aspartate all-in-one doping strategy enables efficient all-perovskite tandems. *Nature* **624**, 69–73 (2023).
- Fu, S. et al. Suppressed deprotonation enables a durable buried interface in tin-lead perovskite for all-perovskite tandem solar cells. *Joule* **8**, 2220–2237 (2024).
- Zhang, Y. et al. Synchronized crystallization in tin-lead perovskite solar cells. *Nat. Commun.* **15**, 6887 (2024).
- Chen, B. et al. Bifacial all-perovskite tandem solar cells. *Sci. Adv.* **8**, eadd0377 (2022).
- Wang, Y. et al. Homogenized contact in all-perovskite tandems using tailored 2D perovskite. *Nature* **635**, 867–873 (2024).
- Zhu, J. et al. Self-assembled hole-selective contact for efficient Sn–Pb perovskite solar cells and all-perovskite tandems. *Nat. Commun.* **16**, 240 (2025).
- Ge, Y. et al. Suppressing wide-angle light loss and non-radiative recombination for efficient perovskite solar cells. *Nat. Photonics* <https://doi.org/10.1038/s41566-024-01570-4> (2025).
- Lin, R. et al. All-perovskite tandem solar cells with 3D/3D bilayer perovskite heterojunction. *Nature* **620**, 994–1000 (2023).
- Ou, Z. et al. Organic ligand engineering for tailoring electron–phonon coupling in 2D hybrid perovskites. *Nano Lett.* **24**, 5975–5983 (2024).
- Shen, Y. et al. Strain regulation retards natural operation decay of perovskite solar cells. *Nature* **635**, 882–889 (2024).
- Gallop, N. P. et al. Ultrafast vibrational control of organohalide perovskite optoelectronic devices using vibrationally promoted electronic resonance. *Nat. Mater.* **23**, 88–94 (2024).
- Zhang, Y. et al. Efficient tin perovskite solar cells via suppressing autoxidation in inert atmosphere. *Small* **20**, 2306115 (2024).
- Duan, H.-G. et al. Photoinduced vibrations drive ultrafast structural distortion in lead halide perovskite. *J. Am. Chem. Soc.* **142**, 16569–16578 (2020).
- Zhou, Y. et al. Giant photostriction in organic–inorganic lead halide perovskites. *Nat. Commun.* **7**, 11193 (2016).
- Wang, J. et al. Enhancing photostability of Sn–Pb perovskite solar cells by an alkylammonium pseudo-halogen additive. *Adv. Energy Mater.* **13**, 2204115 (2023).
- Bai, Y. et al. Decoupling light- and oxygen-induced degradation mechanisms of Sn–Pb perovskites in all perovskite tandem solar cells. *Energy Environ. Sci.* **17**, 8557–8569 (2024).
- Tsai, H. et al. Light-induced lattice expansion leads to high-efficiency perovskite solar cells. *Science* **360**, 67–70 (2018).
- Dey, K. et al. Substitution of lead with tin suppresses ionic transport in halide perovskite optoelectronics. *Energy Environ. Sci.* **17**, 760–769 (2024).
- Lim, V. J.-Y. et al. Air-degradation mechanisms in mixed lead-tin halide perovskites for solar cells. *Adv. Energy Mater.* **13**, 2200847 (2023).
- Hu, S. et al. Optimized carrier extraction at interfaces for 23.6% efficient tin–lead perovskite solar cells. *Energy Environ. Sci.* **15**, 2096–2107 (2022).
- Yamada, Y. & Kanemitsu, Y. Electron-phonon interactions in halide perovskites. *NPG Asia Mater.* **14**, 48 (2022).
- Bischak, C. G. et al. Origin of reversible photoinduced phase separation in hybrid perovskites. *Nano Lett.* **17**, 1028–1033 (2017).
- Lin, R. et al. All-perovskite tandem solar cells with improved grain surface passivation. *Nature* **603**, 73–78 (2022).
- Tong, J. et al. Carrier lifetimes of >1 μs in Sn–Pb perovskites enable efficient all-perovskite tandem solar cells. *Science* **364**, 475–479 (2019).
- Zhu, J. et al. Custom-tailored hole transport layer using oxalic acid for high-quality tin-lead perovskites and efficient all-perovskite tandems. *Sci. Adv.* **10**, eadl2063 (2024).
- Yan, W. et al. Hot-carrier cooling regulation for mixed Sn–Pb perovskite solar cells. *Adv. Mater.* **36**, 2312170 (2024).
- Tan, S. et al. Sustainable thermal regulation improves stability and efficiency in all-perovskite tandem solar cells. *Nat. Commun.* **15**, 4136 (2024).
- Liu, Y. et al. Synergistic immobilization of ions in mixed tin-lead and all-perovskite tandem solar cells. *Nat. Commun.* **16**, 3477 (2025).
- Yang, J. et al. Guiding vertical growth and improving the buried interface of Pb–Sn perovskite films with 2D perovskite seeds for efficient narrow-bandgap perovskite solar cells and tandems. *Energy Environ. Sci.* **18**, 2883–2894 (2025).
- Li, W. et al. Unveiling the nexus between irradiation and phase reconstruction in tin-lead perovskite solar cells. *Nat. Commun.* **16**, 506 (2025).
- Nespoli, J. et al. Metastable oxygen-induced light-enhanced doping in mixed Sn–Pb halide perovskites. *J. Am. Chem. Soc.* **146**, 30860–30870 (2024).
- Yang, X. et al. Understanding and manipulating the crystallization of Sn–Pb perovskites for efficient all-perovskite tandem solar cells. *Nat. Photonics* **19**, 426–433 (2025).
- Liao, X. et al. Methylammonium-free, high-efficiency, and stable all-perovskite tandem solar cells enabled by multifunctional rubidium acetate. *Nat. Commun.* **16**, 1164 (2025).

45. Hong, H. et al. Two-dimensional lead halide perovskite lateral homojunctions enabled by phase pinning. *Nat. Commun.* **15**, 3164 (2024).
46. Zeng, P. et al. Control of hot carrier relaxation in CsPbBr₃ nanocrystals using damping ligands. *Angew. Chem. Int. Ed.* **61**, e202111443 (2022).
47. Heitz, R., Mukhametzhano, I., Stier, O., Madhukar, A. & Bimberg, D. Enhanced polar exciton-LO-phonon interaction in quantum dots. *Phys. Rev. Lett.* **83**, 4654–4657 (1999).
48. Wei, Q. et al. Effect of zinc-doping on the reduction of the hot-carrier cooling rate in halide perovskites. *Angew. Chem. Int. Ed.* **60**, 10957–10963 (2021).
49. Zhang, T. et al. Regulation of the luminescence mechanism of two-dimensional tin halide perovskites. *Nat. Commun.* **13**, 60 (2022).
50. Maufort, A. et al. Structural rigidity, thermochromism and piezochromism of layered hybrid perovskites containing an interdigitated organic bilayer. *Chem. Sci.* **16**, 5662–5675 (2025).
51. Seitz, M. et al. Exciton diffusion in two-dimensional metal-halide perovskites. *Nat. Commun.* **11**, 2035 (2020).
52. Zhang, L. et al. Manipulating local lattice distortion for spectrally stable and efficient mixed-halide blue perovskite LEDs. *Angew. Chem. Int. Ed.* **62**, e202302184 (2023).
53. Zhang, H. et al. Revealing unusual bandgap shifts with temperature and bandgap renormalization effect in phase-stabilized metal halide perovskite thin films. *Adv. Funct. Mater.* **34**, 2302214 (2024).
54. Gao, L. et al. Unveiling strong ion–electron–lattice coupling and electronic antidoping in hydrogenated perovskite nickelate. *Adv. Mater.* **35**, 2300617 (2023).
55. Zhou, Y., Poli, I., Meggiolaro, D., De Angelis, F. & Petrozza, A. Defect activity in metal halide perovskites with wide and narrow bandgap. *Nat. Rev. Mater.* **6**, 986–1002 (2021).
56. Phung, N. et al. Photoprotection in metal halide perovskites by ionic defect formation. *Joule* **6**, 2152–2174 (2022).
57. Ma, C. et al. Unveiling facet-dependent degradation and facet engineering for stable perovskite solar cells. *Science* **379**, 173–178 (2023).
58. Shen, B. et al. A single-molecule van der Waals compass. *Nature* **592**, 541–544 (2021).
59. Shen, B. et al. Atomic imaging of zeolite-confined single molecules by electron microscopy. *Nature* **607**, 703–707 (2022).
60. Liu, S. et al. Triple-junction solar cells with cyanate in ultrawide-bandgap perovskites. *Nature* **628**, 306–312 (2024).
61. Choi, H. S. et al. Molecularly thin, two-dimensional all-organic perovskites. *Science* **384**, 60–66 (2024).
62. Shi, P. et al. Strain regulates the photovoltaic performance of thick-film perovskites. *Nat. Commun.* **15**, 2579 (2024).
63. Chen, C.-H. et al. Full-dimensional grain boundary stress release for flexible perovskite indoor photovoltaics. *Adv. Mater.* **34**, 2200320 (2022).
64. Hutter, E. M. et al. Thermodynamic stabilization of mixed-halide perovskites against phase segregation. *Cell Rep. Phys. Sci.* **1**, 100120 (2020).
65. Islam, J. & Hossain, A. K. M. A. Semiconducting to metallic transition with outstanding optoelectronic properties of CsSnCl₃ perovskite under pressure. *Sci. Rep.* **10**, 14391 (2020).
66. Song, Z. et al. Universal approach for managing iodine migration in inverted single-junction and tandem perovskite solar cells. *Adv. Mater.* **37**, 2410779 (2024).
67. Zhang, Y. et al. Improved fatigue behaviour of perovskite solar cells with an interfacial starch–polyiodide buffer layer. *Nat. Photonics* **17**, 1066–1073 (2023).
68. Niu, T. et al. Stable High-performance perovskite solar cells via grain boundary passivation. *Adv. Mater.* **30**, 1706576 (2018).
69. Zhao, L. et al. Enabling full-scale grain boundary mitigation in polycrystalline perovskite solids. *Sci. Adv.* **8**, eabo3733 (2022).
70. Wang, H. et al. Photomechanically accelerated degradation of perovskite solar cells. *Energy Environ. Sci.* **18**, 2254–2263 (2025).
71. Lu, X. et al. Dynamic reversible oxidation-reduction of iodide ions for operationally stable perovskite solar cells under ISOS-L-3 protocol. *Adv. Mater.* **36**, 2400852 (2024).
72. Luo, J. et al. Improved carrier management via a multifunctional modifier for high-quality low-bandgap Sn–Pb perovskites and efficient all-perovskite tandem solar cells. *Adv. Mater.* **35**, 2300352 (2023).
73. Cao, J. et al. High-performance tin–lead mixed-perovskite solar cells with vertical compositional gradient. *Adv. Mater.* **34**, 2107729 (2022).
74. Li, M. et al. Acceleration of radiative recombination for efficient perovskite LEDs. *Nature* **630**, 631–635 (2024).
75. Chen, H. et al. Quantum-size-tuned heterostructures enable efficient and stable inverted perovskite solar cells. *Nat. Photonics* **16**, 352–358 (2022).

Acknowledgements

This work was financially supported by the National Science Fund for Distinguished Young Scholars (21925506), the National Natural Science Foundation of China (22439004, U21A20331, 81903743, 22279151, 22275004, and 2279151), and the Zhejiang Province “Leading Goose” Plan (2024C01091). Z.G. acknowledges support from the National Science Fund for Distinguished Young Scholars (21925506) and the National Natural Science Foundation of China (22439004, U21A20331, 81903743, 22279151, and 22275004). C.L. acknowledges support from the National Natural Science Foundation of China (2279151) and the Zhejiang Province “Leading Goose” Plan (2024C01091).

Author contributions

C.L. conceived the idea and guided the work. Y.B. and M.Y. fabricated the NBG subcell for device performance. Y.M. fabricated the WBG subcell for device performance. R.T. and J.W. carried out crystal analysis. Y.W. helped with the XPS measurement and data analysis. R.T. and H.P. carried out GIWAXS measurement and data analysis. J.G. calculated the electrostatic potential. B.J. and K.S. calculated DFT simulation calculations. X.L. and S.Z. characterized KPFM test. Z.S. carried out conductivity and associated data analysis. Y.B., C.L. and Z.G. wrote and revised the paper. All the authors contributed to the discussion of the results and the final paper preparation.

Competing interests

The authors declare no competing interests.

Additional information

Supplementary information The online version contains supplementary material available at <https://doi.org/10.1038/s41467-025-62661-6>.

Correspondence and requests for materials should be addressed to Chang Liu or Ziyi Ge.

Peer review information *Nature Communications* thanks René Janssen and the other, anonymous, reviewer(s) for their contribution to the peer review of this work. A peer review file is available.

Reprints and permissions information is available at <http://www.nature.com/reprints>

Publisher’s note Springer Nature remains neutral with regard to jurisdictional claims in published maps and institutional affiliations.

Open Access This article is licensed under a Creative Commons Attribution-NonCommercial-NoDerivatives 4.0 International License, which permits any non-commercial use, sharing, distribution and reproduction in any medium or format, as long as you give appropriate credit to the original author(s) and the source, provide a link to the Creative Commons licence, and indicate if you modified the licensed material. You do not have permission under this licence to share adapted material derived from this article or parts of it. The images or other third party material in this article are included in the article's Creative Commons licence, unless indicated otherwise in a credit line to the material. If material is not included in the article's Creative Commons licence and your intended use is not permitted by statutory regulation or exceeds the permitted use, you will need to obtain permission directly from the copyright holder. To view a copy of this licence, visit <http://creativecommons.org/licenses/by-nc-nd/4.0/>.

© The Author(s) 2025